Cu^{3+} Ion Evaluation and O^{2-} Vacancies Identification in CuO Nanofibers, by XPS Spectroscopy

Manuel Piñon-Espitia *, Saul Verdugo-Miranda, Rafael Verdugo-Miranda, Jose Duarte-Moller *, M. T. Ochoa-Lara

Posted Date: 20 April 2026

doi: 10.20944/preprints202604.1366.v1

Keywords: nanofibers; electrospinning; XPS; CuO

 doi:10.20944/preprints202604.1366.v1

Article

Cu^{3+} Ion Evaluation and O^{2-} Vacancies Identification in CuO Nanofibers, by XPS Spectroscopy

Manuel Piñon-Espitia [1,*], Saul Verdugo-Miranda [2], Rafael Verdugo-Miranda [2], Jose Duarte-Moller [2,*] and M. T. Ochoa-Lara [3]

[1] SECIHTI-Departamento de Física e Ingenierías. Universidad de Sonora, Unidad Regional Sur. Lazáro Cardenas del Río 100, Francisco Villa, 85880, Navojoa and Son. México

[2] Departamento de Física e Ingenierías. Universidad de Sonora, Unidad Regional Sur. Lazáro Cardenas del Río 100, Francisco Villa, 85880, Navojoa and Son. México

[3] Centro de Investigación en Materiales Avanzados, S.C., Laboratorio Nacional de Nanotecnología, Miguel de Cervantes 120, Complejo Industrial Chihuahua, Chihuahua, Chih. 31109 and México

* Correspondence: manuel.pinon@unison.mx

Abstract

The presence of Cu^{3+} cations and oxygen vacancies (V_O) in the electrospun CuO nanofibers was identified by X-ray photoelectron spectroscopy (XPS) from the Cu $2p_{3/2}$ and O 1s core-level spectra, respectively. A Cu^{3+}-related superlattice was observed using nano-beam electron diffraction (NBD). The chemical composition of the two samples thermally treated at 600 °C (CuO600) and 700 °C (CuO700) was further corroborated using the geometrical topofactor method. For comparison, bulk CuO was also analyzed. XPS peak fitting of the Cu 2p and O 1s regions was performed using an SVSC-type background and two-parameter Tougaard function. X-ray diffraction (XRD) confirmed the presence of the tenorite and cuprite phases and enabled crystallite size estimation (FullProf). The average crystallite size ranged from 20.59 ± 0.06 nm to 31.06 ± 0.06 nm, in good agreement with High Resolution Transmission Electron Microscope, HR-TEM, measurements (14.98 ± 0.34 nm and 36.10 ± 0.94 nm). Therefore, we identify that Cu^{3+} and oxygen vacancies in these nanofibers plays a crucial role in optimizing their future applications in the electronic and catalytic fields.

Keywords: nanofibers; electrospinning; XPS; CuO

1. Introduction

Copper oxides, Cu_xO (x = 1–4) [1], are among the most intensively studied advanced materials showing to their relevant optical, electrical, thermal, and magnetic properties. When engineered as nanostructures, these oxide semiconductors can exhibit size- and morphology-dependent behaviors that are not observed in their bulk counterparts [1]. In particular, cuprous oxide (Cu_2O, cuprite) and cupric oxide (CuO, tenorite) in nanofiber form are representative examples of such structure–property relationships [3].

As noted by Sarkar et al. [1] and Collins et al. [2], the presence of Cu^{3+} species and excess holes is correlated, and can contribute to the semiconducting character of CuO. In their study, heat treatments applied to commercial CuO powders, combined with X- Ray Photoelectron Spetroscopy, XPS, and EDP analyses, confirmed a microscopic amount of Cu^{3+} species and holes, which increased with temperature, thereby reinforcing the semiconducting response and increasing dielectric constant. Similar conclusions were reported by Raj et al. [3], who found that the enhanced conductivity of nanostructured CuO was associated with a higher Cu^{3+} concentration together with a small contribution from oxygen vacancies (V_O). XPS is widely used to characterize Cu oxidation states, and the Cu 2p photoemission region is particularly informative for identifying Cu^{3+}-related components. However, Cu 2p spectra are also challenging to interpret because of their complex background, asymmetry, and pronounced multiplet structure, which yields a rich but intricate

 doi:10.20944/preprints202604.1366.v1

spectral envelope compared to many other transition-metal oxides [4–9]. The objective of this work was to evaluate the presence of Cu^{3+} species in onedimensional CuO nanostructures and to examine their relationship with oxygen-vacancyrelated features using XPS. The electrospun CuO nanofibers were subjected to two thermal treatments (600 °C and 700 °C, 4 h each) and compared with a bulk CuO reference. XPS analysis employs recently developed fitting approaches [10]. In addition, the chemical species were quantified and HRTEM observations revealed Cu^{3+}-related superlattice features. Finally, the Rietveld refinement of the X- Ray Diffraction, XRD, data was used to confirm the crystalline phases and estimate the crystallite size. To meet this objective, we combined XPS with nanobeam diffraction (NBD) and Rietveld refinement methods, providing a comprehensive approach to understanding the interaction between Cu^{3+} species and oxygen vacancies in the nanostructures.

2. Experimental Procedure

Polymeric precursor fibers were prepared via electrospinning. First, an 8 wt% poly(vinyl alcohol) (PVA; Sigma-Aldrich, M_w ≈ 130,000, high purity) solution was prepared by dissolving 8 g of PVA in 92 mL of triple-distilled water (resistivity of 1.1 MΩ·cm; J. T. Baker) under magnetic stirring for 24 h at room temperature. A copper precursor solution was prepared by dissolving 1 g of copper(II) acetate (Sigma-Aldrich, 99%) in deionized water and stirring for 4 h at 50 °C. Next, 20 g of PVA solution was added to the copper precursor solution, and the resulting mixture was stirred for 24 h at 600 rpm until a homogeneous, transparent solution was obtained.

Ten milliliters of the final solution were loaded into a syringe mounted on a syringe pump as part of the electrospinning setup. A voltage of 8 kV was applied between the syringe needle and an aluminum foil-covered collector plate placed 20 cm from the needle tip.

Two calcination temperatures were selected based on simultaneous TGA/DSC measurements. The electrospun fibers were heat-treated in air at a heating rate of 10 °C·min^{-1} to 600 °C and 700 °C, yielding the CuO600 and CuO700 samples, respectively. The purpose of these heat treatments was to convert the electrospun precursor fibers Page 5 of 20 into CuO semiconductor nanofibers and remove residual organic components (PVA and acetate-derived species)

3. Characterization

3.1. Structural Characterization by XRD

The crystalline structures of the synthesized CuO nanofibers were analyzed using a high-resolution X-ray diffractometer (PANalytical X'Pert PRO) equipped with an X'Celerator detector. Data were collected using Cu Kα radiation (λ = 1.5418 Å) over the 2θ range of 30–90°, with a step of 0.01° and a counting time of 0.01 s per step. A fine step size of 0.01° allowed the resolution of subtle Cu_2O reflections, enhancing the detection of minor phases and reinforcing the credibility of the results.

The monoclinic CuO structural parameters were refined by Rietveld analysis (leastsquares method) using FullProf Suite [11]. The diffraction peaks were modeled using a pseudo-Voigt profile function. The apparent crystallite size was estimated using the spherical harmonics approach and the Thompson–Cox–Hastings pseudo-Voigt function, including axial-divergence asymmetry and an instrumental resolution file [12].

3.2. Scanning Electron Microscopy (SEM)

Samples were collected by cutting approximately 1 cm² of the aluminum foil used as the collector during electrospinning. Scanning electron microscopy (SEM) micrographs were acquired using a Hitachi SU3500 microscope.

 doi:10.20944/preprints202604.1366.v1

3.3. High-Resolution Transmission Electron Microscopy (HRTEM)

The specimens were prepared by dispersing the synthesized materials in isopropanol (Sigma-Aldrich, 99.8%) for 1 h. A droplet of the suspension was deposited onto 3 mm Ni grids and dried prior to analysis. HRTEM images were acquired using a JEOL JEM-2200FS microscope and processed using DigitalMicrograph [13].

3.4. X-Ray Photoelectron Spectroscopy (XPS)

XPS measurements were performed using a Thermo Scientific ESCALAB X*i* instrument equipped with a monochromatic Al-Kα source (hν = 1486.7 eV). The acquisition parameters were as follows: energy step, 10 eV; energy resolution 0.1 eV, dwell time, 200 ms; 40 scans; takeoff angle, 90°. The CuO nanofibers were mounted on a conductive graphite tape attached to the sample holder. The samples were introduced into the load-lock chamber until a vacuum of approximately 10^{-6} Torr was reached, and measurements were carried out at a base pressure of ~10^{-6} Torr in the analysis chamber. The monochromator was positioned at 45° relative to the photoelectron-collection axis.

3.5. Data analysis

Peak fitting of the Cu 2p and O 1s regions was performed using the AAnalyzer® software, employing a Shirley/SVSC-type background, a two-parameter Tougaard function, and slope correction. The chemical composition was determined using the geometrical topofactor approach (spherical model). Calculations were performed using the Cumpson core–shell model [14,15].

4. Results and Discussion

4.1. XRD Analysis

Structural characterization of the CuO600 and CuO700 samples was carried out by Rietveld refinement of the XRD patterns using FullProf software. The refined patterns are shown in Figure 1, where the shift in the peak positions (dashed line) indicates the changes in the crystalline structure. The calculated profiles (red line) were in good agreement with the experimental data, supporting the reliability of the refinement.

For the CuO600 sample, the refinement indicated a mixed-phase composition consisting of CuO with minor Cu_2O contributions (PDF 75–1531 and 80–1268) (Figure 1b). In contrast, the CuO700 sample exhibited a single CuO (tenorite) phase, consistent with PDF 80–1268.

The refinement results obtained using FullProf [11] are summarized in Table 1. The average crystallite sizes estimated for CuO600 and CuO700 were 31.06 ± 0.06 nm and 20.59 ± 0.06 nm, respectively.

Table 1. Refined lattice parameters for CuO600 and CuO700 obtained by Rietveld analysis using the Thompson–Cox–Hastings pseudo-Voigt peak-shape function with axial-divergence asymmetry.

nanostructure	A (Å)	b (Å)	c (Å)	V (Å³)	R_p (%)	R_{wp} (%)	R_{exp} (%)	χ^2	Y
80-1268	4.6837	3.4226	5.1288	82.2830	-	-	-	-	-
75-1531	4.2678	4.2678	4.2678	77.31	-	-	-	-	-
CuO_{700}	4.6858	3.4230	5.1298	82.2828	4.73	6.35	5.29	1.44	0.4184
CuO_{600}	4.6860	3.4250	5.1343	81.297	12.8	18.2	17.70	1.05	0.41354
	4.2699	4.2699	4.2699	77.774					

 doi:10.20944/preprints202604.1366.v1

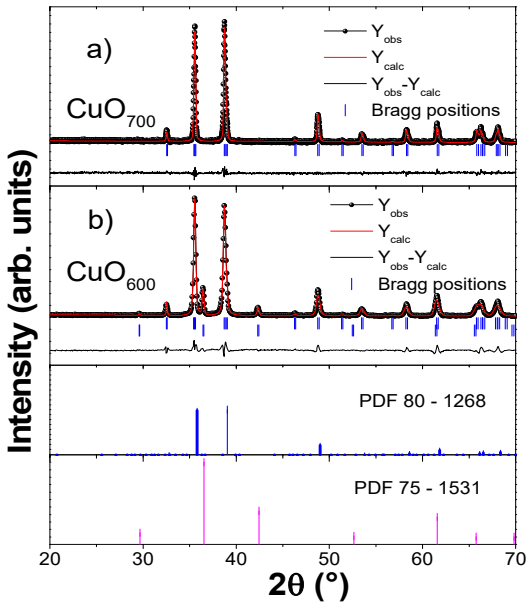

Figure 1. XRD patterns and Rietveld refinements for (a) CuO700 and (b) CuO600, performed using the FullProf Suite [16,17].

4.2. SEM, HR-TEM, and NBD Analysis

The SEM micrograph in Figure 2a shows the as-electrospun polymeric precursor nanofibers (PVA containing copper(II) acetate), forming a randomly oriented fibrous network. Figure 2b presents the diameter distribution of the as-spun nanofibers. Prior to calcination, the precursor fibers consisted of a polymer/metal-salt composite; subsequent heat treatments at 600 °C and 700 °C (yielding CuO600 and CuO700, respectively) promoted the conversion of the precursor into CuO nanofibers through the removal of the organic matrix and decomposition of the acetate species.

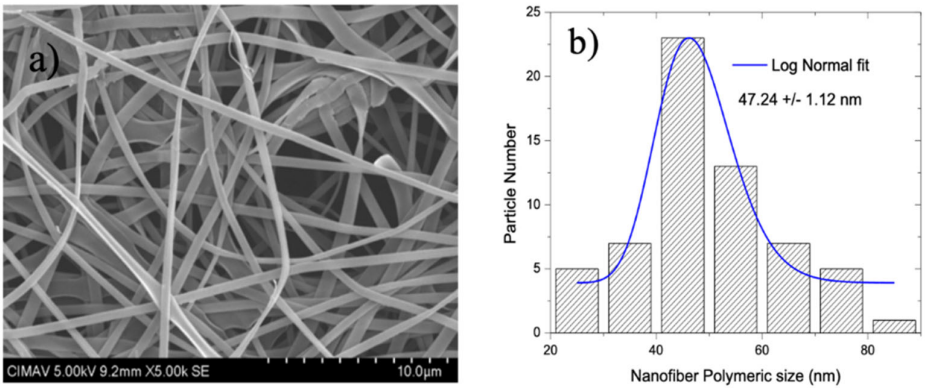

Figure 2. Electrospun precursor fibers. (a) As-spun composite/polymeric nanofibers consisting of PVA loaded with copper(II) acetate, and (b) nanofiber diameter distribution histogram.

The calcined products (CuO nanofibers) were examined by HRTEM and nano-beam electron diffraction (NBD) (Figure 3). The representative morphologies of CuO600 and CuO700 are shown in Figure 3a and Figure 3d, respectively. The corresponding NBD patterns (Figure 3b and Figure 4e) were indexed using CrysTBox [18], confirming the presence of the tenorite (CuO) phase in both samples, in agreement with the XRD results.

 doi:10.20944/preprints202604.1366.v1

In Figure 3b and Figure 3e, the reflections obtained by NBD for CuO600 and CuO700 suggest the presence of Cu^{3+}-related features (highlighted by the yellow circles). In line with previous reports, these features have been described as a superlattice-like contributions associated with additional ionic species. Such contributions are not resolved by XRD, likely because of their low concentration; they may instead reflect local charge density variations, defect-related signatures (e.g., vacancies), and/or minor phases present at trace levels [1,19].

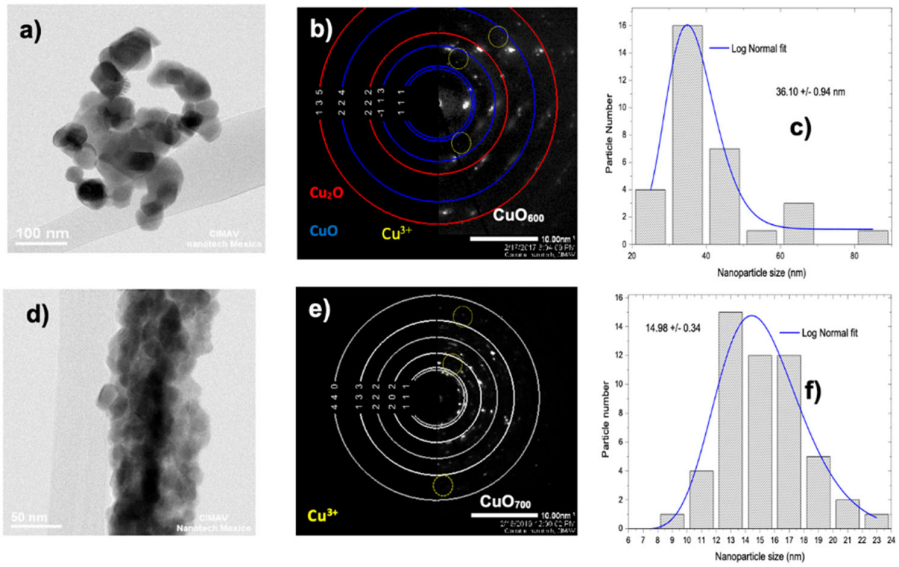

Figure 3. CuO600 nanofibers: (a) TEM micrograph showing the morphology, (b) corresponding nano-beam electron diffraction (NBD) pattern, and (c) particle/nanofiber size distribution histogram. CuO700 nanofibers: (d) TEM micrograph showing the morphology, (e) corresponding NBD pattern, and (f) particle/nanofiber size distribution histogram.

4.3. XPS Analysis and Chemical Composition

The XPS results for CuO600 (Figure 6a,b) and CuO700 (Figure 6 c, d) indicate the presence of Cu^{3+}-related contributions in the Cu 2*p* region (j = 3/2 and j = 1/2), evidenced by features at 936.81 eV and 937.10 eV, respectively. In contrast, these features were not observed for the bulk CuO reference (Figure 6 e, f). An additional contribution associated with the Cu $2p_{3/2}$ shake-up satellite was detected in the CuO700 and reference spectra, but it was absent in the CuO600 spectrum. The origin of this satellite feature remains debated; it has been linked to chemisorption effects and/or an excess of copper species at the surface [1,20,21]. The absence of suppressed satellites in CuO600 suggests a reduced surface disorder rather than a direct compositional change? This alternative explanation invites further critical engagement with spectral data. Table 2 summarizes the peak areas obtained from the fitting of the Cu 2*p* and O 1*s* spectra. The table also lists the binding-energy assignments for the proposed chemical species in the Cu 2p region (Cu^{1+}, Cu^{2+}, and Cu^{3+}) and the O 1s region (O^{2-}) for CuO600, CuO700, and bulk CuO. Only minor variations were observed when using Gaussian–Lorentzian (GL) line shapes (see Table 3), and the fitted parameters remained consistent with previously reported values; a detailed discussion of the fitting theory is beyond the scope of this work [8].

 doi:10.20944/preprints202604.1366.v1

Table 2. Peak areas obtained from fitting the Cu 2*p* and O 1*s* spectra, where A denotes the anion contribution and C the cation contribution.

sample	TakeOff Angle	Cu^{1+} 2*p* C (eV)	O 1s Cu^{1+} A (eV)	Cu 2+ 2*p* A (eV)	O 1s Cu^{2+} A (eV)	Cu^{3+} 2*p* C (eV)	O 1*s* Cu^{3+} A (eV)
CuO_{600}	90	19104.6	12159	16315.5	4590.52	4357.15	1474.3
CuO_{700}	90	6063.7	4543.56	22029.7	5865.18	15944.72	869.603
Bulk	90	5228	7766.1	5035.3	10721	-	-

In Figure 4, the fitted peak areas are compared across the proposed chemical species, showing the relationship between the peak area and the Cu oxidation states (Cu^{1+}, Cu^{2+}, and Cu^{3+}) (Figure 5a). For the Cu^{1+} component, CuO600 and the bulk reference exhibit similar areas (≈ 835.7 a.u.), whereas CuO700 shows a markedly higher value (≈ 19,000 a.u.). For the Cu^{2+} component, the CuO600 and CuO700 samples fall in the range of approximately 16,000–22,000 a.u., whereas the bulk sample shows a substantially lower area (≈ 5,035 a.u.). Finally, the Cu^{3+}-related component exhibits comparable areas in CuO600 and CuO700 (≈ 11,587.6 a.u.) and was not observed in the bulk reference. Overall, this indicates a trend toward an oxygen-rich but Cu^{1+}-dominant chemical landscape, particularly in the CuO700 sample, where the presence of Cu^{1+} was significantly more pronounced.

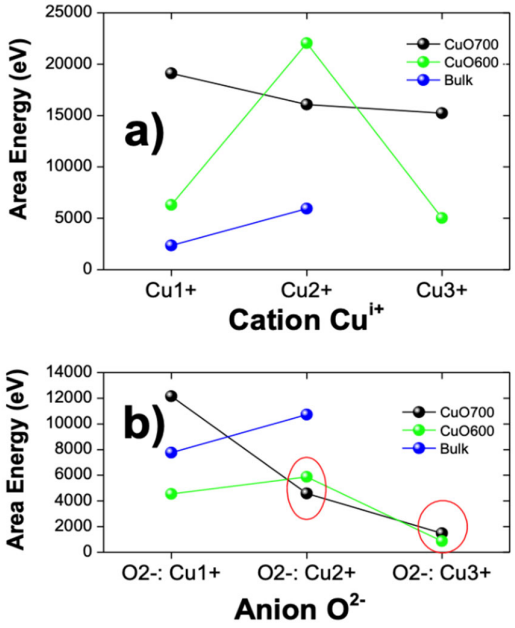

Figure 4. Schematic representation of the fitted peak areas derived from the Cu 2*p* and O 1*s* XPS spectra.

In Figure 4b, the O^{2-} anion contribution is compared with the previously discussed cationic components through the ratios O^{2-}:Cu^{i} (with $i = 1^+, 2^+, 3^+$). The O^{2-}:Cu^{3+} ratio yielded values of approximately 2,000 a.u. for both CuO600 and CuO700. For O^{2-}:Cu^{1+}, the minimum value was observed for CuO700 (≈ 4,000 a.u.), whereas the bulk reference and CuO600 showed higher values of approximately 8,000 a.u. and 12,000 a.u., respectively. In addition, O^{2-}:Cu^{2+} for CuO600 and CuO700 lies in the range of approximately 4,000–6,000 a.u., whereas the bulk sample reaches a maximum of approximately 10,000 a.u.

Cu 2p XPS spectra and the spin–orbit splitting between the Cu $2p_{3/2}$ and Cu $2p_{1/2}$ components for CuO600 (a,b), CuO700 (c,d), and bulk reference samples (e,f), respectively.

On the other hand, the spin–orbit splitting between the Cu 2*p* XPS spectra and the spin– orbit splitting between the Cu 2p3/2 and Cu $2p_{1/2}$ components for CuO600 (a,b), CuO700 (c,d), and the bulk reference sample (e,f). The Cu $2p_{3/2}$ and Cu $2p_{1/2}$ components are shown in Figure 5b, d, and f. A slight decrease in the binding energy was observed, which may be associated with changes in the electronic

 doi:10.20944/preprints202604.1366.v1

structure of the Cu 2p levels (with degeneracy) [22]. The splitting of the main Cu 2*p* peaks was estimated from the measured positions of the Cu^{2+} components and the corresponding Cu $2p_{3/2}$ shake-up satellite features, yielding values in close agreement with those reported by Pauly, Tougaard, and Yubero [22].

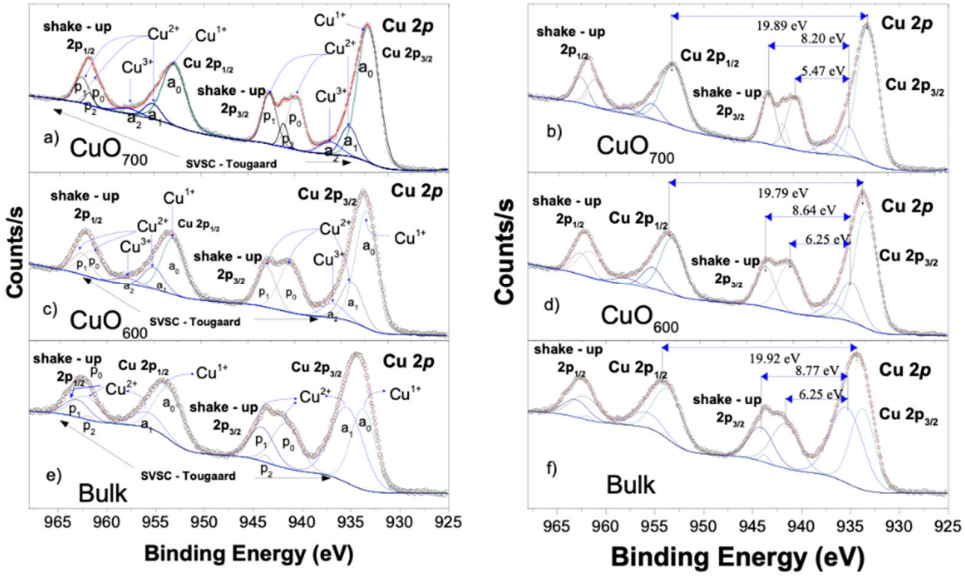

Figure 5. Cu 2p XPS spectra and the spin–orbit splitting between the Cu $2p_{3/2}$ and Cu $2p_{1/2}$ components for CuO600 (a,b), CuO700 (c,d), and the bulk reference sample (e,f), respectively.

Table 3 lists the binding energies obtained from the fitting of the main Cu 2p peaks of the CuO600, CuO700, and bulk samples. The corresponding fitting errors are 3.7242×10^{-5} eV, 2.5698×10^{-5} eV, and 3.05987×10^{-5} eV, respectively.

The fit parameters associated with the SVCS Shirley and Tougaard backgrounds were consistent with previously reported values. [1,3,22–24] The Gaussian and Lorentzian broadening components exhibited values that were characteristic of nanostructured samples (Table 3). In contrast, the bulk reference sample showed no Lorentzian contribution, and the Gaussian broadening remains ≤ 3.0 eV, which is consistent with its larger (micrometric/macroscopic) structural scale.

Table 4 summarizes the background parameters used in the deconvolution of the Cu 2p spectra and their associations with the proposed chemical species. Background modelling was performed using the SVCS Shirley-type background together with a Tougaard background, which enabled the reliable assignment of the chemical components in the nanostructured samples. The background energy parameters obtained for each Cu 2p spectrum (Table 4) were within the ranges previously reported. [10,25–28] In addition, the degree of oxygen homogeneity was evaluated using the Shirley-type slope parameter. [5].

Table 3. Parameters used for fitting the Cu 2p region for each sample.

Sample	Date	Peak	$2p_{3/2}$ BE (eV)	$2p_{1/2}$ BE (eV)	Shake-up $2p_{3/2}$ BE (eV)	Peak Width FWHM	
						Gaussian (eV)	Lorentzian (eV)
Bulk	Cu 2*p*	a_1	933.72	953.58		3.78[a]-3.30[b]	0.085
		a_2	935.35	955.8		2.79[a]-3.41[b]	0.085
		p_1			941.59	3.22	0.085
		p_2			944.11	2.86	0.085
		p_3			943.72	1.00	0.085
CuO_{600}	Cu 2*p*	a_1	933.37	953.19		2.48	0.270
		a_2	934.91	955.21		1.86	0.270

 doi:10.20944/preprints202604.1366.v1

		a_3	936.81	957.91		2.48	0.270
		p_1			941.19	1.97	0.270
		p_2			943.66	1.74	0.270
CuO_{700}	Cu 2*p*	a_1	933.19	953.09		2.48	0.270[a]–0.514[b]
		a_2	935.17	955.28		1.86	0.270[a]–0.059[b]
		a_3	937.1	957.67		2.48	0.270[a]–0.514[b]
		p_1			940.64	1.97	0.27
		p_2			943.37	1.74	0.27
		p_3			941.91	1.00	0.27

Table 4. Parameters obtained from the SVCS Shirley background, Tougaard background, and slope term, derived from the optimized fitting of the Cu 2p and O 1s spectra.

Sample	Shirley type SVSC (eV^{-1})	Shirley type Tougaard (eV^{-1})	Shirley type Slope (eV^{-1})
Bulk	0.028, 0.045	2000	0.0040
CuO_{600}	0.035, 0.048, 0.035	2000	0.0025
CuO_{700}	0.054, 0.068, 0.75	2000	0.0038

Figure 6 shows the O 1*s* spectra of each sample and their relationship with the Cu 2*p* chemical components. The observed asymmetry could be associated with oxygen coordination in the tenorite (CuO) structure. [29] Unlike previous studies that fitted O 1s using only Gaussian functions, [3,23,29] the O 1s envelopes were fitted using a combined Gaussian–Lorentzian (GL) line shape, yielding an optimized fit consistent with the spectral broadening behavior [5,23].

For CuO, the main lattice oxygen contribution (O2-) appears at 529.50 eV (CuO600), 529.30 eV (CuO700), and 529.76 ± 0.05 eV (bulk). Additional components at 531.15 eV (CuO600), 531.33 eV (CuO700), and 530.66 ± 0.05 eV (bulk) are commonly assigned to higher-binding-energy oxygen-related species, and have also been reported as signatures associated with oxygen-deficient regions (oxygen vacancies). [3,29] Finally, features at 533.13 eV (CuO600) and 532.84 ± 0.01 eV (bulk) are attributed to surface oxygen species. [3] In the bulk sample, an additional peak near ~536 eV is observed, which can be attributed to adventitious carbon/CO2-related species, likely arising from the carbon tape used during the XPS measurements.

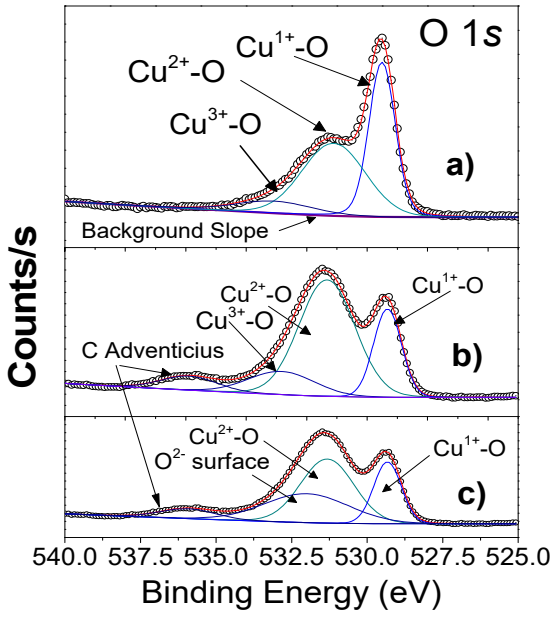

Figure 6. O 1s spectra for (a) CuO600, (b) CuO700, and (c) the bulk CuO sample.

 doi:10.20944/preprints202604.1366.v1

The stoichiometries calculated using the topofactor method were, for CuO600: $Cu_{1.02}O_{1.16}$, $Cu_{2.22}O_{2.12}$, $Cu_{2.22}O_{3.03}$, for CuO_{700} were $Cu_{1.02}O_{1.15}$, $Cu_{2.06}O_{2.03}$, $Cu_{2.05}O_{3.19}$ and for the bulk sample: $Cu_{0.97}O_{1.02}$, $Cu_{2.43}O_{2.01}$, with an estimated error of ~4%. These values are supported by the geometrical core–shell model (cylindrical geometry) proposed in the literature. [14,15,30]

Table 5 summarizes the chemical compositions derived from the primary XPS signals (Cu 2p and O 1s). The observed non-stoichiometric ratios may arise from excess oxygen, heat treatments carried out under non-controlled atmospheres, and/or structural defects, including oxygen vacancies. [23,32,33].

Table 5. Quantification of the primary XPS signals for the Cu 2p and O 1s peaks. Fitting peaks for the Chemical species Cu^{1+}, Cu^{2+}, Cu^{3+} and the variation with the calcination temperatures.

Fitting peaks for the Chemical species Cu^{1+}, Cu^{2+}, Cu^{3+} and the variation with the calcination temperatures.										
Heat Treatment	Chemical Species		Peak Binding Energy BE (eV)	Peak Binding Energy BE (eV)	CuO	X_{CuO}	X_C	I_1/I_2	A	SF
700 ºC	Cu^{+1}	O^{-2}	933.19	529.50	Cu^{+1}–O^{-2}	0.33–0.54		0.35–0.64	0.98	$Cu_{1.02}O_{1.16}$
	Cu^{+2}	O^{-2}	935.17	531.15	Cu^{+2}–O^{-2}	0.34–0.65		0.75–1.29	0.98	$Cu_{2.22}O_{2.15}$
	Cu^{+3}	O^{-2}	937.1	533.13	Cu^{+3}–O^{-2}	0.33–0.58		0.75–0.46	0.98	$Cu_{2.22}O_{3.03}$
600 ºC	Cu^{+1}	O^{-2}	933.36	529.3	Cu^{+1}–O^{-2}	0.33–0.54		0.35–0.64	0.98	$Cu_{1.02}O_{1.15}$
	Cu^{+2}	O^{-2}	934.91	531.33	Cu^{+2}–O^{-2}	0.33–0.57		1.05–0.64	0.98	$Cu_{2.06}O_{2.03}$
	Cu^{+3}	O^{-2}	936.81	532.84	Cu^{+3}–O^{-2}	0.33–0.14		1.05–2.37	0.98	$Cu_{2.05}O_{3.19}$
	C -O	O^{-2}	284.84	536.01	C–O		1.00	0.35	0.98	
Bulk	Cu^{+1}	O^{-2}	933.33	529.76	Cu^{+1}–O^{-2}	0.35–0.48		0.35–0.51	0.98	$Cu_{0.97}O_{1.02}$
	Cu^{+2}	O^{-2}	936.06	530.66	Cu^{+2}–O^{-2}	0.81–0.54		1.66–1.36	0.98	$Cu_{2.43}O_{2.01}$
	C-O	O^{-2}	284.96	536.1	C–O		1.00	0.45	0.98	

5. Conclusions

XRD analysis using the FullProf suite revealed that CuO600 consists of a mixture of Cu_2O (cuprite) and CuO (tenorite) phases forming nanofibers with an average crystallite size of 31.06 ± 0.06 nm, whereas CuO700 shows single-phase CuO (tenorite) nanofibers with an average crystallite size of 20.59 ± 0.06 nm. The NBD analysis of the CuO600 and CuO700 nanofibers revealed superlattice reflections associated with the presence of Cu^{3+}. [1,19] The indexed diffraction patterns further corroborated the mixed-phase sample (Cu2O–cuprite and CuO–tenorite) for CuO600 and a single-phase CuO–tenorite sample for CuO700. XPS enabled the identification of the main oxidation states (Cu1+, Cu2+, Cu3+, and O2 −). In particular, the Cu 2p spectra support the presence of Cu3+ in both nanofiber samples, whereas this contribution was absent in the bulk CuO reference. The Cu 2p spin–orbit splitting values are consistent with those reported previously. [1,3,7,22,23,34,35] In Page 16 of 20 addition, the measured Cu 2p spin–orbit splitting (ΔE = E2p1/2–E2p3/2) was 19.79 eV for CuO600, 19.89 eV for CuO700, and 19.92 eV for bulk CuO, suggesting changes in spin– orbit coupling related to exchange interactions involving the 3d states. [25] The fitted spectra also indicate non-stoichiometry, likely arising from calcination under noncontrolled atmospheres, consistent with the compositional analysis. [3,14,15] Finally, the O 1s spectra show that CuO600 exhibits a more pronounced oxygen-vacancy related component (≈ 531.33 eV) and a higher Cu3+-related intensity than CuO700, which is in agreement with previous reports. [3,29] The bulk reference lacks the Cu^{3+} component near ~937 eV; however, it strongly contributes to the oxygen vacancy region.

Data Availability Statement: The original contributions presented in this study are included in the article. Further inquiries can be directed to the corresponding authors.

Acknowledgments: The author S. Verdugo-Miranda thanks the Ph.D. SECIHTI scholarship grants No. 4003867. We acknowledge the financial support from SECIHTI (grant CPFIA-251111-9369). The authors also thank M.C. Luis Gerardo Silva-Vidaurri, manager of the XPS facility, for support during the measurements.

 doi:10.20944/preprints202604.1366.v1

Conflicts of Interest: The authors declare no conflict of interest.

References

1. S. Sarkar, P. Kumar Jana, B. K. Chaudhuri, and H. Sakata, "Copper (II) oxide as a giant dielectric material Synthesis of Cu 2 O from CuO thin films: Optical and electrical properties Copper " II… oxide as a giant dielectric material," Cit. Appl. Phys. Lett. J. Appl. Phys. Appl. Phys. Lett. Appl. Phys. Lett. Nickel Oxide, Their Mix. Cryst. J. Appl. Phys., vol. 8911, no. 10, pp. 212905–2703, 2006. https://doi.org/10.1063/1.2393001.
2. Collins, B.; Desisto, W.; Kershaw, R.; Dwight, K.; Wold, A. Preparation and characterization of Cu(II) oxide. *J. Less Common Met.* **1989**, *156*, 341–346. https://doi.org/10.1016/0022-5088(89)90429-3.
3. Raj, A.A.; Biju, V. Nanostructured CuO: Facile synthesis, optical absorption and defect dependent electrical conductivity. *Mater. Sci. Semicond. Process.* **2017**, *68*, 38–47. https://doi.org/10.1016/j.mssp.2017.05.008.
4. Végh, J. The Shirley background revised. *J. Electron Spectrosc. Relat. Phenom.* **2006**, *151*, 159–164. https://doi.org/10.1016/j.elspec.2005.12.002.
5. Cabrera-German, D.; Gomez-Sosa, G.; Herrera-Gomez, A. Accurate peak fitting and subsequent quantitative composition analysis of the spectrum of Co 2 *p* obtained with Al Kα radiation: I: cobalt spinel. *Surf. Interface Anal.* **2016**, *48*, 252–256. https://doi.org/10.1002/sia.5933.
6. Herrera-Gomez, A.; Bravo-Sanchez, M.; Ceballos-Sanchez, O.; Vazquez-Lepe, M.O. Practical methods for background subtraction in photoemission spectra. *Surf. Interface Anal.* **2014**, *46*, 897–905. https://doi.org/10.1002/sia.5453.
7. Salvia, A.; E Castle, J. The intrinsic asymmetry of photoelectron peaks: dependence on chemical state and role in curve fitting. *J. Electron Spectrosc. Relat. Phenom.* **1998**, *95*, 45–56. https://doi.org/10.1016/s0368-2048(98)00205-9.
8. Desimoni, E.; Casella, G.; Cataldi, T.; Malitesta, C. A comparison of some asymmetrical line shapes for XPS data analysis. *J. Electron Spectrosc. Relat. Phenom.* **1989**, *49*, 247–261. https://doi.org/10.1016/0368-2048(89)85012-1.
9. L. G. M. Herrera-Gomez, Alberto., Dagoberto Cabrera-German., Anthony D. Dutoi., Milton Vazquez Lepe., Servando Aguirre-Tostado., Piero Pianetta., Dennis Nordlund., Orlando Cortazar-Martinez., Alejandro Torres-Ochoa.,Oscar Ceballos-Sanchez., "Modulation of the intensity of the Shirley background of the Cr 3p spectra with photon energies around the Cr 2p edge," J. Electron Spectros. Relat. Phenomena, 2017.
10. A. H.-G. et Al, "Formation of Si1+ in the early stages of the oxidation of the Si [001] 2 x 1 surfaces," Vaccum Sci. Tecnol. A Vaccum, Surfaces, Film., vol. 34, no. 020601, pp. 1–4, 2016.
11. Rodríguez-Carvajal, J. Recent advances in magnetic structure determination by neutron powder diffraction. *Phys. B Condens. Matter* **1993**, *192*, 55–69. https://doi.org/10.1016/0921-4526(93)90108-i.
12. Rodríguez-Carvajal, J. Recent advances in magnetic structure determination by neutron powder diffraction. *Phys. B Condens. Matter* **1993**, *192*, 55–69. https://doi.org/10.1016/0921-4526(93)90108-i.
13. K. W. Eliceiri, "Micrograph Digital," NIH Image to ImageJ 25 years image Anal. Nat. Methods, vol. 9, p. 671, 2009.
14. Shard, A.G. A Straightforward Method For Interpreting XPS Data From Core–Shell Nanoparticles. *J. Phys. Chem. C* **2012**, *116*, 16806–16813. https://doi.org/10.1021/jp305267d.
15. Shard, A.G.; Wang, J.; Spencer, S.J. XPS topofactors: determining overlayer thickness on particles and fibres. *Surf. Interface Anal.* **2009**, *41*, 541–548. https://doi.org/10.1002/sia.3044.
16. Rodríguez-Carvajal, J. Recent advances in magnetic structure determination by neutron powder diffraction. *Phys. B Condens. Matter* **1993**, *192*, 55–69. https://doi.org/10.1016/0921-4526(93)90108-i.
17. Roisnel, T.; Rodríquez-Carvajal, J. WinPLOTR: A Windows Tool for Powder Diffraction Pattern Analysis. *Mater. Sci. Forum* **2001**, *378-381*, 118–123. https://doi.org/10.4028/www.scientific.net/msf.378-381.118.
18. A. J. Klinger, M., "Crystallographic Tool Box (CrysTBox): automated tools for transmission electron microscopists and crystallographers," Appl. Crystallogr., 2015.
19. Zheng, X.G.; Xu, C.N.; Tomokiyo, Y.; Tanaka, E.; Yamada, H.; Soejima, Y. Observation of Charge Stripes in Cupric Oxide. *Phys. Rev. Lett.* **2000**, *85*, 5170–5173. https://doi.org/10.1103/physrevlett.85.5170.
20. Dongliang, Y.; Chuannan, G.; Youwei, D. Preparation and characterization of CuO nanowire arrays. *J. Semicond.* **2009**, *30*. https://doi.org/10.1088/1674-4926/30/7/072003.

 doi:10.20944/preprints202604.1366.v1

21. Chusuei, C.C.; Brookshier, M.A.; Goodman, D.W. Correlation of Relative X-ray Photoelectron Spectroscopy Shake-up Intensity with CuO Particle Size. *Langmuir* **1999**, *15*, 2806–2808. https://doi.org/10.1021/la9815446.
22. F. Y. N. Pauly, S. Tougaard, "Determination of the Cu 2p primary excitation spectra for Cu, Cu2O and CuO," Surf. Sci., vol. 620, pp. 17–22, 2014.
23. M. B.-S. J. A. Torres - Ochoa, Diego Fernando Mulato - Gòmez, Dagoberto Cabrera - Germàn, "Detailed analysis of the photoemission spectra of copper films with coexistent Cu1+, Cu2+ and Cu3+ oxidation states," in Detailed analysis of the photoemission spectra of copper films with coexistent Cu1+, Cu2+ and Cu3+ oxidation states, 2017, pp. 125–126.
24. Hauschild, D.; Handick, E.; Göhl-Gusenleitner, S.; Meyer, F.; Schwab, H.; Benkert, A.; Pohlner, S.; Palm, J.; Tougaard, S.M.; Heske, C.; et al. Band-Gap Widening at the Cu(In,Ga)(S,Se)$_2$Surface: A Novel Determination Approach Using Reflection Electron Energy Loss Spectroscopy. *ACS Appl. Mater. Interfaces* **2016**, *8*, 21101–21105. https://doi.org/10.1021/acsami.6b06358.
25. Leapman, R.D.; Grunes, L.A.; Fejes, P.L. Study of theL_{23}edges in the3$d$transition metals and their oxides by electron-energy-loss spectroscopy with comparisons to theory. *Phys. Rev. B* **1982**, *26*, 614–635. https://doi.org/10.1103/physrevb.26.614.
26. Tougaard, S.; Sigmund, P. Influence of elastic and inelastic scattering on energy spectra of electrons emitted from solids. *Phys. Rev. B* **1982**, *25*, 4452–4466. https://doi.org/10.1103/physrevb.25.4452.
27. A. Herrera-Gomez, "The Peak-Shirley Background (Shirley background in overlapping peaks)."
28. Castle, J.; Chapman-Kpodo, H.; Proctor, A.; Salvi, A. Curve-fitting in XPS using extrinsic and intrinsic background structure. *J. Electron Spectrosc. Relat. Phenom.* **2000**, *106*, 65–80. https://doi.org/10.1016/s0368-2048(99)00089-4.
29. Gao, D.; Yang, G.; Li, J.; Zhang, J.; Zhang, J.; Xue, D. Room-Temperature Ferromagnetism of Flowerlike CuO Nanostructures. *J. Phys. Chem. C* **2010**, *114*, 18347–18351. https://doi.org/10.1021/jp106015t.
30. Baer, D.R.; Engelhard, M.H.; Johnson, G.E.; Laskin, J.; Lai, J.; Mueller, K.; Munusamy, P.; Thevuthasan, S.; Wang, H.; Washton, N.; et al. Surface characterization of nanomaterials and nanoparticles: Important needs and challenging opportunities. *J. Vac. Sci. Technol. A* **2013**, *31*, 050820. https://doi.org/10.1116/1.4818423.
31. Kim, S.Y.; Khanal, D.; Tharkar, P.; Kalionis, B.; Chrzanowski, W. None of us is the same as all of us: Resolving heterogeneity of stem cell-derived extracellular vesicles using single-vesicle, nanoscale characterization with highresolution resonance enhanced atomic force microscope infrared spectroscopy (AFM-IR). *Nanoscale Horiz.* **2018**, *3*, 430–438. https://doi.org/10.1039/x0xx00000x.
32. Debbichi, L.; de Lucas, M.C.M.; Pierson, J.F.; Krüger, P. Vibrational Properties of CuO and Cu_4O_3 from First-Principles Calculations, and Raman and Infrared Spectroscopy. *J. Phys. Chem. C* **2012**, *116*, 10232–10237. https://doi.org/10.1021/jp303096m.
33. Zeng, J.; Xu, J.; Wang, S.; Tao, P.; Hua, W. Ferromagnetic behavior of copper oxide-nanowire-covered carbon fibre synthesized by thermal oxidation. *Mater. Charact.* **2009**, *60*, 1068–1070. https://doi.org/10.1016/j.matchar.2009.03.012.
34. Debbichi, L.; de Lucas, M.C.M.; Pierson, J.F.; Krüger, P. Vibrational Properties of CuO and Cu_4O_3 from First-Principles Calculations, and Raman and Infrared Spectroscopy. *J. Phys. Chem. C* **2012**, *116*, 10232–10237. https://doi.org/10.1021/jp303096m.
35. Iqbal, M.; Thebo, A.A.; Shah, A.H.; Iqbal, A.; Thebo, K.H.; Phulpoto, S.; Mohsin, M.A. Influence of Mn-doping on the photocatalytic and solar cell efficiency of CuO nanowires. *Inorg. Chem. Commun.* **2017**, *76*, 71–76. https://doi.org/10.1016/j.inoche.2016.11.023.